Chemical/Physical Pressure Tunable Spin-Transition Temperature and Hysteresis in a Two-Step Spin Crossover Porous Coordination Framework

Jian-Bin Lin,[†] Wei Xue,[†] Bao-Ying Wang,[†] Jun Tao,[‡] Wei-Xiong Zhang,[†] Jie-Peng Zhang,*[,†] and Xiao-Ming Chen*[,†]

[†]MOE Key Laboratory of Bioinorganic and Synthetic Chemistry, State Key Laboratory of Optoelectronic Materials and Technologies, School of Chemistry and Chemical Engineering, Sun Yat-Sen University, Guangzhou 510275, China

[‡]State Key Laboratory of Physical Chemistry of Solid Surfaces, College of Chemistry and Chemical Engineering, Xiamen University, Xiamen 361005, China

Ⓢ Supporting Information

ABSTRACT: A two-dimensional (2D) square-grid type porous coordination polymer [Fe(bdpt)$_2$]·guest (**1**·g, Hbdpt = 3-(5-bromo-2-pyridyl)-5-(4-pyridyl)-1,2,4-triazole) with isolated small cavities was designed and constructed as a spin-crossover (SCO) material based on octahedral Fe^{II}N$_6$ units and an all-nitrogen ligand. Three guest-inclusion forms were successfully prepared for **1**·g (**1**·EtOH for g = ethanol, **1**·MeOH for g = methanol, **1** for g = Null), in which the guest molecules interact with the framework as hydrogen-bonding donors. Magnetic susceptibility measurements showed that **1**·g exhibited two-step SCO behavior with different transition temperatures (**1**·EtOH < **1**·MeOH < **1**) and hysteresis widths (**1**·EtOH > **1**·MeOH > **1** ≈ 0). Such guest modulation of two-step spin crossover temperature and hysteresis without changing two-step state in a porous coordination framework is unprecedented. X-ray single-crystal structural analyses revealed that all two-step SCO processes were accompanied with interesting symmetry-breaking phase transitions from space group of $P2_1/n$ for all high-spin Fe(II), to $P\bar{1}$ for ordered half high-spin and half low-spin Fe(II), and back to $P2_1/n$ for all low-spin Fe(II) again by lowering temperature. The different SCO behaviors of **1**·g were elucidated by the steric mechanism and guest–host hydrogen-bonding interactions. The SCO behavior of **1**·g can be also controlled by external physical pressure.
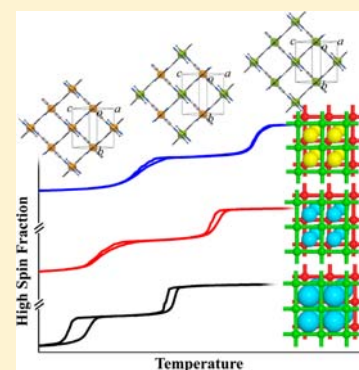
INTRODUCTION

Spin crossover (SCO) is an electron configuration transition between the high-spin (HS) and low-spin (LS) states under external perturbations, such as temperature, light, and magnetic field.[1−5] The spin transition temperature, hysteresis, and number of steps are important criteria for SCO materials.[6−8] Different SCO behaviors of coordination complexes may be rationalized on the basis of ligand field theory.[9] A large number of SCO materials have been synthesized, most of which are based on a typical local coordination structure Fe^{II}N$_6$.[10,11] However, the rational design and fabrication of materials with SCO property remain elusive because multiple weak bonding interactions, such as intermolecular hydrogen bonding, π−π stacking, and van der Waals interactions, show cooperative effects on SCO behaviors.[10,11] As exemplified by the fact that many Fe^{II}N$_6$ type compounds do not exhibit SCO properties, the topology and connectivity of extended structures also greatly influence SCO behaviors.[12] Systematic comparison of structurally highly related compounds is very important to understand the above-mentioned subtle effects on SCO behaviors.

Porous coordination polymers (PCPs), providing identical/similar host framework structures and variable guest species, can serve as a suitable platform for studying the structure–property correlations. The guest molecules could be altered to evaluate the effect of host–guest interactions on SCO behaviors.[13−17] The electrostatic and/or weak bonding interactions of guest molecules were found to enhance the electronic cooperativity of spins and increase the widths of hysteresis loops.[18,19] For example, in [Fe(NCS)$_2$(bpbd)$_2$] (SCOF-2, bpbd = 2,3-bis(4′-pyridyl)-2,3-butanediol), guest molecule with smaller dielectric constant gives rise to higher SCO temperature.[13] Steric effect of guest molecules may also play an important role in controlling SCO properties. For example, the Hofmann-type PCP [Fe(pyrazine)Ni(CN)$_4$] included with bulkier guest molecule exhibits higher SCO temperature.[14] The guest-induced structure change has not been observed for these compounds, probably because they possess large channels and/or rigid framework structures.

In principle, PCPs with small cavity size and multiple coordination networks, such as two-dimensional (2D) packing and three-dimensional (3D) interpenetrated structures, could supply more significant structure response for different guest

Table 1. Crystal Data and Structure Refinements for 1·EtOH and 1·MeOH at Various Temperatures

	1·EtOH				1·MeOH			1	
formula	$C_{26}H_{20}Br_2FeN_{10}O$				$C_{25}H_{18}Br_2FeN_{10}O$			$C_{24}H_{14}Br_2FeN_{10}$	
formula weight	704.19				690.16			658.12	
crystal system	monoclinic	triclinic	monoclinic	monoclinic	triclinic	monoclinic	monoclinic	triclinic	monoclinic
space group	$P2_1/n$	$P\bar{1}$	$P2_1/n$	$P2_1/n$	$P\bar{1}$	$P2_1/n$	$P2_1/n$	$P\bar{1}$	$P2_1/n$
T/K	293(2)	136(2)	103(2)	293(2)	153(2)	109(2)	293(2)	173(2)	97(2)
a/Å	8.819(3)	8.6854(9)	8.5888(16)	8.6888(10)	8.5530(4)	8.4660(12)	8.5942(8)	8.5092(5)	8.4361(11)
b/Å	14.702(5)	14.4819(14)	14.149(3)	14.9313(18)	14.6729(10)	14.437(2)	14.9817(14)	14.6903(10)	14.4264(18)
c/Å	10.458(3)	10.4064(10)	10.554(2)	10.1493(12)	10.1236(8)	10.1757(14)	10.1941(10)	10.2033(6)	10.2503(13)
α/deg	90	89.184(8)	90	90	89.052(6)	90	90	88.809(5)	90
β/deg	103.894(6)	103.298(8)	102.868(3)	104.513(2)	104.019(6)	103.465(2)	103.976(2)	103.415(5)	102.885(3)
γ/deg	90	89.357(8)	90	90	89.622(5)	90	90	89.486(5)	90
V/Å³	1316.3(7)	1273.6(2)	1250.3(4)	1274.7(3)	1232.40(14)	1209.5(3)	1273.7(2)	1240.25(13)	1216.1(3)
Z	2	2	2	2	2	2	2	2	2
D_c/g cm^{-3}	1.777	1.836	1.871	1.798	1.860	1.895	1.716	1.762	1.797
μ/mm^{-1}	3.651	8.792	3.844	3.768	9.071	3.971	3.764	8.949	3.942
R_1 $[I > 2\sigma(I)]^a$	0.0537	0.0842	0.0425	0.0470	0.0608	0.0454	0.0544	0.0636	0.0516
wR_2 $[I > 2\sigma(I)]^b$	0.1179	0.2330	0.1074	0.1188	0.1552	0.1142	0.1203	0.1575	0.1242
R_1 (all data)	0.1050	0.1041	0.0612	0.0672	0.0716	0.0625	0.0955	0.1012	0.0747
wR_2 (all data)	0.1447	0.2422	0.1194	0.1337	0.1619	0.1262	0.1455	0.1679	0.1419
GOF	1.003	1.009	1.002	1.005	1.006	1.007	1.002	1.002	1.002

$^a R_1 = \sum ||F_o| - |F_c||/\sum |F_o|$. $^b wR_2 = [\sum w(F_o{}^2 - F_c{}^2)^2/\sum w(F_o{}^2)^2]^{1/2}$.

molecules.[20,21] We and others have demonstrated that 3-(2-pyridyl)-5-(4-pyridyl)-1,2,4-triazolate (Hdpt) type ligands can enforce octahedral divalent metal ions to adopt all-nitrogen coordination and produce microporous metal azolate frameworks (MAFs) with 4-connected topologies (packing of 2D **sql** or interpenetration of 3D **nbo**).[12,22−25] Moreover, the dipyridyl-substituted triazolate ligands possess excess nitrogen acceptors exposing on the pore surfaces,[24] which could be used to tune SCO behavior by interaction with guest molecules. Although a large number of SCO PCPs have been synthesized, most of them exhibit only one-step SCO behavior. Two-step and even multistep spin transition may be better for ternary memory and multiswitch devices, and increase the storage density.[7] In this contribution, we employ Fe(II) and a new triazolate ligand to construct a 2D MAF with a two-step SCO behavior accompanying crystallographic phase transition, which is remarkably different with the reported α-[Fe(dpt)$_2$].[12] More importantly, its SCO behavior could be tuned by different guest molecules included in the micropores without changing two-step spin transition, which has not been observed in porous coordination frameworks.

EXPERIMENTAL SECTION

Materials and Methods. Commercially available reagents were used as received without further purification. 3-(5-Bromo-2-pyridyl)-5-(4-pyridyl)-1,2,4-triazole (Hbdpt) was prepared according to a reported method.[26] Elemental analyses (C, H, N) were performed on a Perkin-Elmer 240 elemental analyzer. Thermal gravimetric analyses were performed under N$_2$ using a TA TGA Q50 system. Powder X-ray diffraction (PXRD) patterns were recorded on a Bruker D8 Advance diffractometer (Cu Kα). Analytical pyrolysis was carried out with a CDS Pyroprobe model 5200 pyrolyzer with a platinum coil probe and gas chromatography−mass spectrometry using GC-2010 and GCMS-QP2010 Plus. Magnetic measurements were performed using a Quantum Design SQUID MPMS magnetometer working in 2.0−300 K range with a magnetic field of 5000 Oe. Pressure applied externally to the samples for the Quantum Design MPMS measure-ment platform was done using an EasyLab Mcell 10 hydrostatic pressure cell.

Crystal Structure Determination. Intensity data were collected on a Bruker Apex CCD area-detector diffractometer (Mo Kα) or an Oxford Gemini S Ultra diffractometer (Cu Kα). Absorption corrections were applied by using the multiscan program SADABS[27] or spherical harmonics implemented in SCALE3 ABSPACK scaling algorithm. The crystal structures of 1·EtOH (136(2) K), 1·MeOH (153(2) K), and 1 (173(2) K) were refined as about 50:50 twin components. The structures were solved with direct methods and refined with a full-matrix least-squares technique with the SHELXTL program package.[28] Anisotropic thermal parameters were applied to all non-hydrogen atoms except the guest molecules. The organic hydrogen atoms were generated geometrically.

Synthesis of [Fe(bdpt)$_2$]·EtOH (1·EtOH). A mixture of Fe-(ClO$_4$)$_2$·6H$_2$O (0.036 g, 0.1 mmol), Hbdpt (0.060 g, 0.2 mmol), LiCl·H$_2$O (0.009 g, 0.1 mmol), ethanol (EtOH) (3 mL), and N,N-dimethylformamide (DMF) (1 mL) was placed in a 10-mL thick glass tube. The tube was filled with dinitrogen, sealed and heated at 393 K for 5 days, and then cooled spontaneously to room temperature. Pure crystals of 1·EtOH were isolated in about 57% yield. Anal. Calcd (%) for $C_{26}H_{20}Br_2FeN_{10}O$: C, 44.35; H, 2.86; N, 19.89. Found: C, 44.07; H, 2.78; N, 19.78.

Synthesis of [Fe(bdpt)$_2$]·MeOH (1·MeOH). The procedure used for the preparation of 1·EtOH was employed, but with a replacement of EtOH by methanol (MeOH) as solvent. Pure crystals of 1·MeOH were isolated in about 51% yield. Anal. Calcd (%) for $C_{25}H_{18}Br_2FeN_{10}O$: C, 43.51; H, 2.63; N, 20.30. Found: C, 43.78; H, 2.68; N, 20.36.

RESULTS AND DISCUSSIONS

Synthesis and Structure. Solvothermal reaction of Hbdpt and Fe(ClO$_4$)$_2$ in EtOH or MeOH mixed with DMF produced phase-pure crystals of [Fe(bdpt)$_2$]·EtOH (1·EtOH) and [Fe(bdpt)$_2$]·MeOH (1·MeOH), respectively. The guest-free phase [Fe(bdpt)$_2$] (1) could only be obtained by desolvation treatment of 1·EtOH or 1·MeOH (Supporting Information, Figures S1−S4). The chemical formulas of these compounds have been confirmed by elemental analysis, thermogravimetry
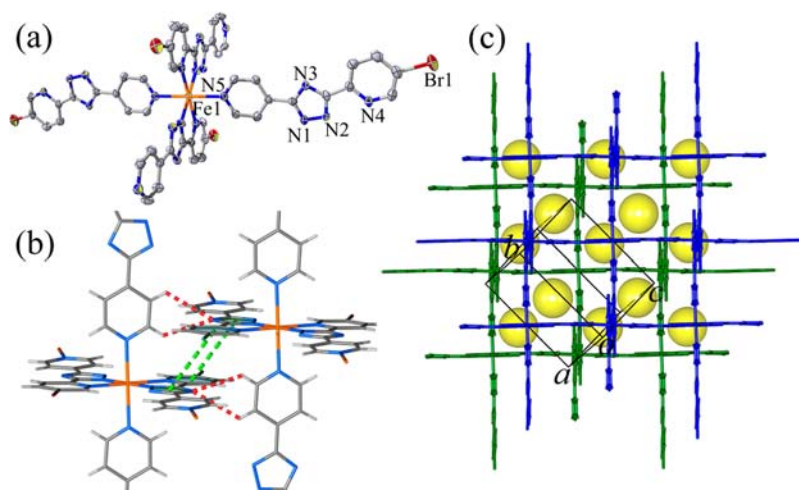
Figure 1. (a) Coordination environment of the Fe^{II} atom, (b) supramolecular interactions of two adjacent layers (hydrogen-bonding and $\pi-\pi$ stacking interactions are highlighted as red and green dashed sticks, respectively) and (c) offset packing of two adjacent square-grid coordination layers (discrete cavities are shown as yellow spheres) of **1**·g.

(TG), pyrolysis-gas chromatography–mass spectrometry (pyrolysis-GC/MS) analysis, and single-crystal X-ray diffraction studies.

The three different guest-inclusion forms of **1**·g all crystallize in the space group $P2_1/n$ at room temperature, containing half an Fe atom, one bdpt$^-$ ligand, and half a guest molecule (Table 1). The Fe atom adopts an N$_6$ octahedral coordination geometry from two chelating sites of two bdpt$^-$ and two pyridyl ends from another two bdpt$^-$ ligands in a *trans*-configuration (Figure 1a), giving rise to 2D square-grid (**sql**) sheets parallel to the [101] plane, which are the same to those of α-[M(dpt)$_2$] (M^{II} = Mn^{II} or Fe^{II}).[12,24] As shown in Table 2, the average Fe–N bond length is 2.202(4)–2.205(3) Å, falling in the range of normal HS Fe^{II}–N bond lengths.[10] The bdpt$^-$ ligands are nearly vertical to the **sql** plane (81.68(5)–83.38(4)°). The sheets interdigitate in an offset fashion (1/3 offset between adjacent layers) with $\pi-\pi$ stacking interactions (3.360(13)–3.44(2) Å) and C–H···N hydrogen bonds (C···N 3.272(7)–3.441(7) Å) to form the 3D packing structure (Figure 1b), whereas α-[M(dpt)$_2$] exhibit a stagger fashion (1/2 offset between adjacent layers). Because the grid sizes (neighboring Fe···Fe distances 10.5 Å) are about three times of normal face-to-face $\pi-\pi$ stacking separations (3.4 Å), small cavities are retained between interlayer spaces to host guest molecules (Figure 1c and Supporting Information, Figure S5). It should be noted that the triazolate 1- and 4-nitrogens are not involved in coordination. While the former is partially exposed on the pore surface, the latter is completely covered by an adjacent layer by forming double C–H···N hydrogen bonds (Figure 1b).

In the crystal structures of **1**·EtOH and **1**·MeOH, the solvent guests are 2-fold symmetrically disordered. The O–H···N hydrogen-bonding distances are 2.93(2) and 3.05(2) Å in **1**·EtOH and **1**·MeOH, respectively, meaning a stronger hydrogen bond for the larger guest EtOH. Generally, the steric hindrance effect prevents molecules from approaching each other, especially for the bulky ones. However, when guest molecules are confined in the small cages as in the case of **1**, the longer/larger one could squash in the small corners more effectively, resulting in shorter contacts with the hydrogen-bonding acceptor (i.e., the uncoordinated 1-nitrogen) (Scheme 1). The size difference of guest molecules could be observed

from the three crystal structures. While the intralayer Fe···Fe distances are very similar among the three forms (10.5422(6)–10.578(2) Å), the interlayer distance of **1**·EtOH (5.88 Å) is obviously longer than those of **1**·MeOH (5.72 Å) and **1** (5.73 Å). The corresponding closest $\pi-\pi$ face-to-face distances are 3.44(2), 3.360(13), and 3.400(10) Å for **1**·EtOH, **1**·MeOH, and **1**, respectively. For the interlayer C–H···N hydrogen-bonding interactions, the closest C···N distances are 3.401(7), 3.310(5), and 3.272(7) Å for **1**·EtOH, **1**·MeOH, and **1**, respectively. The void volumes are 11.9%, 10.9%, and 9.9% in **1**·EtOH, **1**·MeOH, and **1**, respectively. The gradually altered packing and weak bonding structures of **1**·g may serve as a good candidate to investigate the steric and/or electronic effect of guest molecules on SCO behaviors.

Magnetic Studies. Magnetic susceptibilities measured at ambient pressure revealed different SCO behaviors for **1**·EtOH, **1**·MeOH, and **1** (Figures 2 and 3). The molar fractions of HS versus total Fe^{II} ions are plotted in Figure 2. At first glance, all three forms display two-step abrupt spin transition processes with different hysteresis widths. While two-step SCO systems are useful as multiswitch and ternary information storage materials, the number of two-step SCO materials is still limited, especially those with hysteresis.[29–35] The dense compound α-[Fe(dpt)$_2$] exhibits only one-step SCO behavior with a hysteresis of 6.8 K.[12] The difference between **1**·g and similar compounds may be ascribed to the electrostatic dipole effect of the bromine group[36,37] and packing interaction.[33,38]

Taking **1**·EtOH as an example, the $\chi_M T$ value is about 3.80 cm^3·K·mol^{-1} between 300 and 160 K, indicating a HS state (Figure 3a). Upon cooling, the value suddenly drops in the range 160–153 K ($T_{1/2(1)\downarrow}$ = 154 K) and reaches an intermediate plateau of about 2.20 cm^3·K·mol^{-1} between 153 and 116 K, corresponding to an HS-LS state with γ_{HS} = 58%. The $\chi_M T$ value abruptly drops again in the range 117–109 K ($T_{1/2(2)\downarrow}$ = 113 K) to about 0.85 cm^3·K·mol^{-1} and continues to decrease and reaches 0.19 cm^3·K·mol^{-1} at 2 K. This may be mainly attributed to a residual high spin Fe(II) population because some Fe(II) ions on the crystal surface are not fully coordinated by bdpt$^-$ ligands and/or trace paramagnetic impurity is present in the sample. Subsequent measurements in the warming mode revealed two abrupt increases centered at $T_{1/2(2)\uparrow}$ = 121 K and $T_{1/2(1)\uparrow}$ = 158 K, resulting in two

Table 2. Selected Structural Data for 1·EtOH and 1·MeOH at Various Temperatures[a]

distance (Å)/angle (deg)	1·EtOH^HS	1·EtOH^IP	1·EtOH^LS	1·MeOH^HS	1·MeOH^IP	1·MeOH^LS	1^HS	1^IP	1^LS
T/K	293(2)	136(2)	103(2)	293(2)	153(2)	109(2)	293(2)	173(2)	97(2)
Fe(1)−N(1)	2.200(5)	2.008(8)	2.021(3)	2.201(3)	2.020(6)	2.015(4)	2.209(5)	2.025(6)	2.011(4)
Fe(1)−N(2)	2.107(4)	1.990(9)	1.992(3)	2.100(3)	1.981(7)	1.983(3)	2.095(4)	1.982(7)	1.971(4)
Fe(1)−N(5) or Fe(1)−N(10)	2.304(5)	2.074(9)	2.089(3)	2.313(3)	2.089(7)	2.078(4)	2.302(4)	2.085(7)	2.074(4)
Fe(2)−N(5)^#1		2.313(10)			2.289(8)			2.289(7)	
Fe(2)−N(6)		2.198(8)			2.195(6)			2.189(6)	
Fe(2)−N(7)		2.123(10)			2.086(7)			2.103(7)	
$\langle d_{Fe1-N} \rangle$	2.204(5)	2.024(9)	2.034(3)	2.205(3)	2.030(7)	2.025(4)	2.202(4)	2.031(7)	2.019(4)
$\langle d_{Fe2-N} \rangle$		2.211(9)			2.190(7)			2.194(7)	
$\sum_{Fe1}$	58.1(2)	41.6(3)	41.2(1)	60.1(1)	43.6(3)	42.3(1)	61.9(2)	45.2(2)	41.4(2)
$\sum_{Fe2}$		58.4(3)			58.8(3)			62.0(2)	
Fe···Fe distance	10.578(2)	10.4111(10), 10.4463(9)	10.317(1)	10.5552(8)	10.3637(7), 10.4420(7)	10.2928(9)	10.5422(6)	10.3515(6), 10.4474(6)	10.2825(8)
C···N of C−H···N	3.401(7), 3.441(7)	3.32(1), 3.36(1), 3.36(1), 3.42(1)	3.306(5), 3.362(5)	3.310(5), 3.345(5)	3.22(1), 3.26(1), 3.27(1), 3.32(1)	3.211(5), 3.260(5)	3.272(7), 3.336(7)	3.25(1), 3.28(1), 3.30(1), 3.36(1)	3.210(6), 3.281(6)
$\pi-\pi$ distance	3.44(2)	3.35(2)	3.320(15)	3.360(13)	3.345(18), 3.322(17)	3.272(14)	3.400(10)	3.340(13), 3.321(14)	3.278(10)
interlayer distance	5.88	5.86	5.88	5.72	5.69	5.71	5.73	5.73	5.75
O···N of O−H···N	2.93(2)	2.88(2), 2.90(2)	2.901(9)	3.05(2)	3.01(2), 3.06(3)	3.03(1)			
guest size/Å³	49.8				34.1				

[a]Symmetry code #1 − x, 2 − y, 2 − z.

Scheme 1. Larger/Longer Guest Molecule May Get Closer to the Corners of a Small Cavity
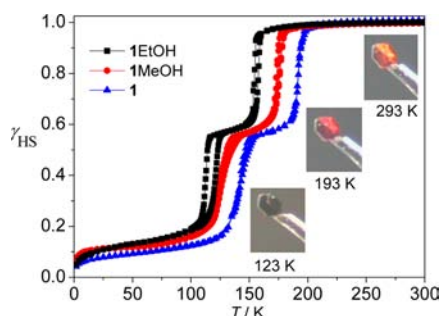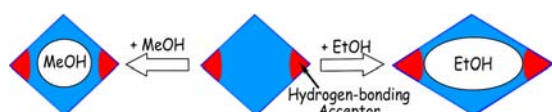
Figure 2. Temperature dependence of molar fraction of HS (γ_{HS}) for **1**·EtOH, **1**·MeOH, and **1** derived from the magnetic susceptibility measurements. (The molar fraction of HS at 300 K is regarded as 1.0. Inset: photographs of crystal **1** at different temperatures).

parallelogram hysteresis of 8 and 4 K widths, respectively. As shown in Figure 2 and Table 3, the $T_{1/2}$ values of the three guest-inclusion forms span a range of about 36 K and follow the order of **1**·EtOH < **1**·MeOH < **1**, while their hysteresis widths follow **1**·EtOH > **1**·MeOH > **1**. Such phenomena can be explained well by the differences of guest size/volume and guest−host hydrogen-bonding interactions. Large guest molecules are expected to hinder the contraction of the host framework and stabilize the HS state toward lower temperatures.[14] Guest hydrogen-bonding donors would also be expected to reduce the electron density of the host framework and lower the SCO temperature.[39,40] The change of hysteresis width (**1**·EtOH > **1**·MeOH > **1**) may not be attributed to the interlayer $\pi−\pi$ stacking or C−H···N hydrogen-bonding interactions because these weak bonding distances follow **1**·EtOH > **1**·MeOH ≈ **1** (Table 2). Alternatively, electrostatic contributions from guest−host hydrogen-bonding interactions would be suggested to explain the hysteresis phenomena.[18,41] The O−H···N hydrogen-bonding interaction in **1**·EtOH is stronger than that in **1**·MeOH, which may lead to the wider hysteresis loops in **1**·EtOH.[42] These intermolecular interactions would be regarded as "chemical pressure" that modulate the strength of coordination field and play an important role in tuning the SCO behavior. It is noteworthy that such dramatic guest-induced change of two-step SCO temperature and hysteresis is unprecedented, although a few porous frameworks showing guest modulated one-step SCO behavior have been reported.[13,14,43,44] Moreover, all the three forms exhibited a remarkably wide plateau of 35−37 K indicating that the intermediate phase could be stable.[45]

Spin-transition properties of SCO compounds can be effectively modified with not only the application of "chemical pressure" but also physical hydrostatic pressure. For **1**·EtOH, the thermal hysteresis width of the first-step increases to be 15 K at a pressure of 3.52 kbar, as shown in Figure 3a and Table 3, which is almost four times of that at 1 bar, while the hysteresis width of the second-step almost doubles. At 4.83 kbar, two large hysteresis loops are still observed, and the average $T_{1/2(1)}$ distinctly increases by 23 K with respect to that at ambient
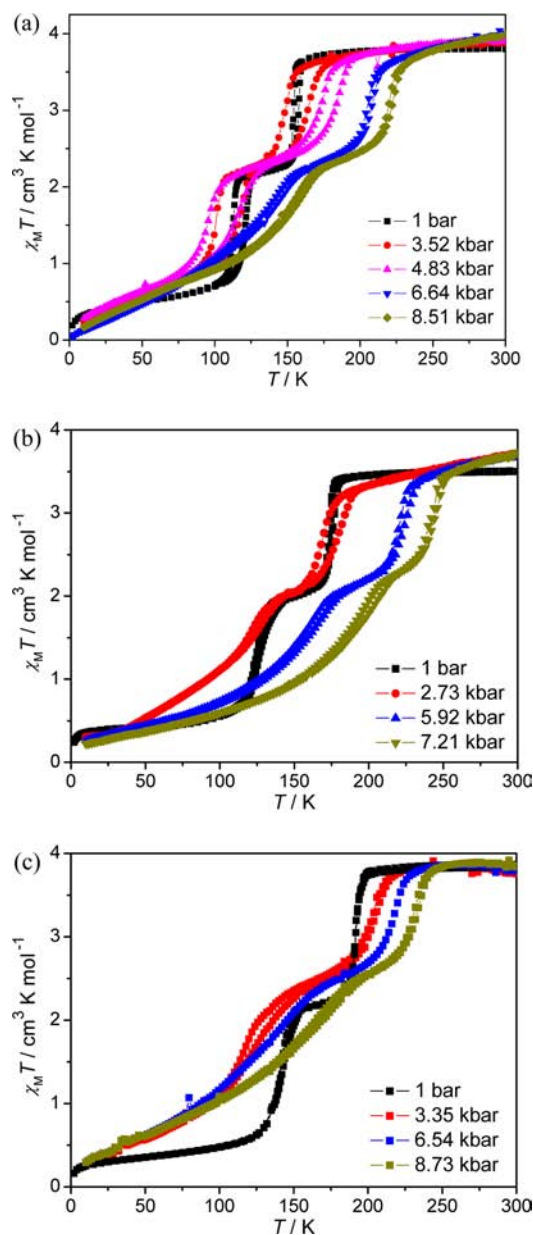
Figure 3. Pressure effect on the SCO behaviors of (a) **1**·EtOH, (b) **1**·MeOH, and (c) **1**.

pressure. However, $T_{1/2(2)}$ even lowers down by increasing the physical pressure up to 4.83 kbar, which is unexpected because additional pressure favors low spin states of SCO compounds and increase the SCO temperature.[46] At 6.64 kbar, $T_{1/2(1)}$ and $T_{1/2(2)}$ increase by 52 and 16 K compared with those at ambient pressure, respectively, whereas the hysteresis width diminishes to be 3−4 K. By increasing the pressure up to 8.51 kbar, only an obvious elevation of SCO temperature is found. Similar effects also appeared in **1**·MeOH (Figure 3b and Table 3). However, the physical pressure applied on **1** only increases the spin-transition temperature in the first-step region and diminishes the difference of the two-step transition (Figure 3c and Table 3). The abrupt spin transition at ambient pressure becomes more and more gradual as the pressure increases, which demonstrates that additional pressure enhances the ligand field around the Fe(II) ion and reduces the difference of the chemical environments between adjacent Fe(II) sites.[47]

Table 3. SCO Temperature Parameters of 1·EtOH, 1·MeOH, and 1 at Various Pressures[a]

compounds	P/kbar	first step				second step			
		$T_{1/2\downarrow}$/K	$T_{1/2\uparrow}$/K	$T_{1/2(1)}$/K	hysteresis width/K	$T_{1/2\downarrow}$/K	$T_{1/2\uparrow}$/K	$T_{1/2(2)}$/K	hysteresis width/K
1·EtOH	0.001	154	158	156	4	113	121	117	8
	3.52	150	165	158	15	101	117	109	16
	4.83	174	184	179	10	96	114	105	18
	6.64	206	209	208	3	131	135	133	4
	8.51	221	223	222	2	146	149	148	3
1·MeOH	0.001	173	176	175	3	127	128	128	1
	2.73	173	184	179	11	119	121	120	2
	5.92	222	226	224	4	154	158	156	4
	7.21	243	245	244	2	183	187	185	4
1	0.001	192	192	192	0	143	144	144	1
	3.35	200	202	201	2	115	120	118	5
	6.54	215	216	216	1	123	127	125	4
	8.73	229	231	230	2	142	144	143	2

[a]$T_{1/2} = (T_{1/2\downarrow} + T_{1/2\uparrow})/2$.

The nonlinear increase of SCO temperature is probably relevant to the synergy between physical pressure and structural flexibility associated with such as hydrogen bonding and $\pi-\pi$ stacking interactions.[48] Under external physical pressure, the enhanced electrostatic interactions could even, to a significant extent, broaden the hysteresis.

Structure Variation. Multistep SCO behavior often accompanies phase transitions of crystal structures.[31,35,49,50] We determined the crystal structures for all three guest-inclusion forms at low temperatures, which show phase-transitions follow well with the two-step SCO behaviors, that is, from monoclinic ($P2_1/n$) at room temperature to triclinic ($P\bar{1}$) at intermediate temperature and then back to monoclinic ($P2_1/n$) at about 100 K, as shown in Figure 4 and Table 1. Taking
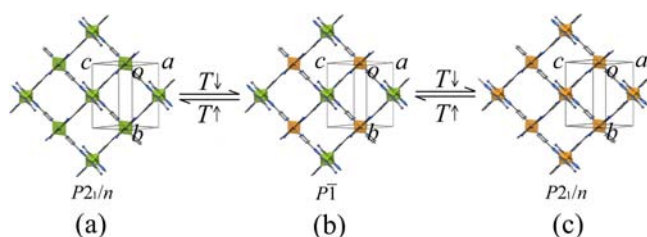
Figure 4. Transitions of HS (a), LS-HS (b), and LS (c) crystal structures of **1·EtOH** (Green and orange polyhedra represent the HS and LS Fe(II) ions, respectively).

1·EtOH as an example, at 136(2) K, only a slightly contraction of the unit cell is observed relative to that determined at room temperature, but the crystal symmetry is reduced to $P\bar{1}$, containing two crystallographically distinct Fe(II) ions with average Fe−N bond lengths of 2.024(9) and 2.211(9) Å, respectively, suggesting an ordered LS-HS state. At 103(2) K, the unit cell is further contracted, and the space group converts back to $P2_1/n$ with average Fe−N bond length of 2.034(3) Å, which is slightly longer than a typical LS Fe^{II}−N bond,[10] indicating an incomplete spin transition and corresponding well with the magnetic susceptibility. The changes of octahedral distortion parameters of the Fe^{II}N$_6$ coordination spheres[42] ($\sum$ = 58.1(2)°, 41.6(3)/58.4(3)°, and 41.2(1)° at HS, LS-HS, and LS states, respectively) are consistent with the spin-state assignments based on Fe−N bond distances. A distinct color change of the crystal from orange to red, and further to dark

red upon lowering of temperature also indicates a two-step transition (Figure 2 inset). Similar phenomena were also observed for **1·MeOH** and **1** (Table 2).

The lowering of temperature not only decreases the Fe−N bond lengths for each compound, but also reduces the distances of adjacent Fe⋯Fe and $\pi-\pi$ stacking (Table 2). For **1·EtOH**, the intralayer adjacent Fe⋯Fe distance is reduced from 10.578(2) Å at 293 K to 10.4111(10) and 10.4463(9) Å at 136 K to 10.317(1) Å at 103 K. The corresponding distances of $\pi-\pi$ stacking interactions are reduced from 3.44(2) to 3.35(2) to 3.320(15) Å by lowering the temperature. The host−guest hydrogen-bonding interaction is also strengthened with decreasing temperature. The O⋯N distances of O−H⋯N are 2.93(2), 2.88(2)−2.90(2), and 2.901(9) Å at 293, 136, and 103 K, respectively. However, the layer spacing (measured from the planes of layer through Fe(II) ions) does not show obvious temperature dependence and even increases by lowering the temperature below 136 K. This may be ascribed to the extrusion in 2D layers and extension in the third direction.

The single-crystallographic data revealed similar phase transition and framework contraction among the three guest inclusion forms by lowering temperature. More importantly, it can be concluded that the size of EtOH (4.16 × 4.27 × 6.33 Å^3)[51] is obviously larger than that of the cavity in the guest-free state, while MeOH (3.81 × 4.18 × 4.95 Å^3)[51] is similar (Figure 5). For example, the unit-cell volume, $\pi-\pi$, C⋯N distances of
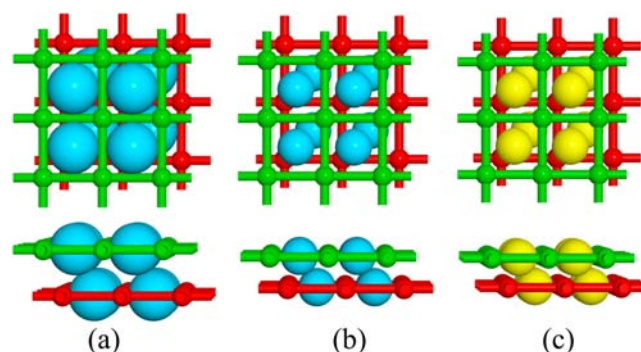
Figure 5. Schematic presentations of the frameworks in (a) **1·EtOH**, (b) **1·MeOH**, and (c) **1** viewed vertical (up) and parallel (down) to the layers (blue and yellow balls represent the guest molecules and cages, respectively).
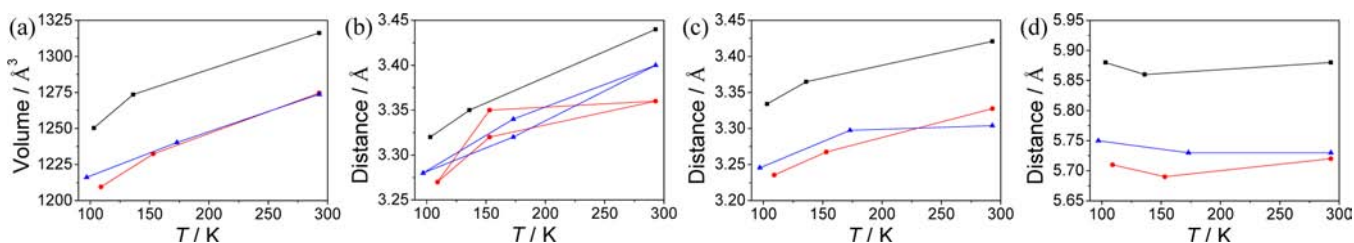
Figure 6. (a) Unit-cell volume, (b) interlayer $\pi-\pi$ distances, (c) average interlayer C⋯N (C−H⋯N), and (d) interlayer spacing of **1**·EtOH (black), **1**·MeOH (red), and **1** (blue) at different temperatures.

C−H⋯N, and interlayer distances in **1**·MeOH and **1** are very similar, and are obviously smaller than those in **1**·EtOH (Figure 6 and Table 2). In other words, the guest molecules could apply another type of "chemical pressure" on the host frameworks and retard the contraction of the crystal lattice upon the transition from HS to LS state. This effect can also explain why the guest included compounds are hard to be compressed by external pressure, and therefore hard to be in the LS state. In summary, the magnetic properties of **1**·EtOH could be largely ascribed to the size effect of EtOH molecules, while those of **1**·MeOH could primarily result from the hydrogen-bonding interaction.

CONCLUSIONS

Through introducing different guest molecules in the isolated cavities of the supramolecular framework of a new 2D porous coordination polymer based on Fe(II) ion and an all-nitrogen ligand, the influence of guest molecule size and guest−host hydrogen-bonding interaction on SCO behavior were studied. Interestingly, these compounds undergo unprecedented guest molecules and physical pressure controlled two-step SCO behaviors. The two-step SCO processes of these materials accompany not only drastic changes in color from orange to red and further to dark red upon cooling but also drastic symmetry changes of the crystal. X-ray single-crystal diffraction studies showed that the size of the guest molecule plays the most important role on the SCO properties through a steric mechanism, when the guest molecule is large enough compared to the cavity size. In this case, the large guest molecule retard the framework contraction induced by the HS to LS Fe−N bond shortening and decreases the SCO temperature. Our results also illustrate the importance of guest−host hydrogen bonding on SCO behavior including the width of hysteresis loops and SCO temperature. Therefore, this study offers an insight into the nature of the steric mechanism and electrostatic contributions on SCO temperature and thermal hysteresis through modifying the guest molecules in a porous coordination polymer, which may be instructive for tuning the properties of SCO materials.

ASSOCIATED CONTENT

Ⓢ Supporting Information

The additional structural data, TGA curves, Pyrolysis-GC/MS plot, PXRD, crystal structures, as well as X-ray crystallographic files in CIF format. This material is available free of charge via the Internet at http://pubs.acs.org.

AUTHOR INFORMATION

Corresponding Author

*E-mail: zhangjp7@mail.sysu.edu.cn (J.-P.Z.), cxm@mail.sysu.edu.cn (X.-M.C.). Fax: +86 20 8411-2245.

Notes
The authors declare no competing financial interest.

REFERENCES

(1) Kahn, O. *Molecular Magnetism*; VCH, Weinheim, Germany, 1993.
(2) Real, J. A.; Andrés, E.; Munoz, M. C.; Julve, M.; Granier, T.; Bousseksou, A.; Varret, F. *Science* **1995**, *268*, 265.
(3) Halder, G. J.; Kepert, C. J.; Moubaraki, B.; Murray, K. S.; Cashion, J. D. *Science* **2002**, *298*, 1762.
(4) Gütlich, P.; Goodwin, H. A. *Top. Curr. Chem.* **2004**, *233*, 1.
(5) Sato, O.; Tao, J.; Zhang, Y. Z. *Angew. Chem., Int. Ed.* **2007**, *46*, 2152.
(6) Halcrow, M. A. *Chem. Soc. Rev.* **2011**, *40*, 4119.
(7) Nihei, M.; Tahira, H.; Takahashi, N.; Otake, Y.; Yamamura, Y.; Saito, K.; Oshio, H. *J. Am. Chem. Soc.* **2010**, *132*, 3553.
(8) Kahn, O. *Science* **1998**, *279*, 44.
(9) Hauser, A. *Top. Curr. Chem.* **2004**, *233*, 49.
(10) Olguin, J.; Brooker, S. *Coord. Chem. Rev.* **2011**, *255*, 203.
(11) Muñoz, M. C.; Real, J. A. *Coord. Chem. Rev.* **2011**, *255*, 2068.
(12) Bao, X.; Liu, J. L.; Leng, J. D.; Lin, Z. J.; Tong, M. L.; Nihei, M.; Oshio, H. *Chem.—Eur. J.* **2010**, *16*, 7973.
(13) Neville, S. M.; Halder, G. J.; Chapman, K. W.; Duriska, M. B.; Moubaraki, B.; Murray, K. S.; Kepert, C. J. *J. Am. Chem. Soc.* **2009**, *131*, 12106.
(14) Southon, P. D.; Liu, L.; Fellows, E. A.; Price, D. J.; Halder, G. J.; Chapman, K. W.; Moubaraki, B.; Murray, K. S.; Letard, J. F.; Kepert, C. J. *J. Am. Chem. Soc.* **2009**, *131*, 10998.
(15) Ohba, M.; Yoneda, K.; Agusti, G.; Munoz, M. C.; Gaspar, A. B.; Real, J. A.; Yamasaki, M.; Ando, H.; Nakao, Y.; Sakaki, S.; Kitagawa, S. *Angew. Chem., Int. Ed.* **2009**, *48*, 4767.
(16) Agusti, G.; Ohtani, R.; Yoneda, K.; Gaspar, A. B.; Ohba, M.; Sanchez-Royo, J. F.; Munoz, M. C.; Kitagawa, S.; Real, J. A. *Angew. Chem., Int. Ed.* **2009**, *48*, 8944.
(17) Ohtani, R.; Yoneda, K.; Furukawa, S.; Horike, N.; Kitagawa, S.; Gaspar, A. B.; Carmen Munoz, M.; Real, J. A.; Ohba, M. *J. Am. Chem. Soc.* **2011**, *133*, 8600.
(18) Kepenekian, M.; Le Guennic, B.; Robert, V. *J. Am. Chem. Soc.* **2009**, *131*, 11498.
(19) Létard, J.-F.; Guionneau, P.; Codjovi, E.; Lavastre, O.; Bravic, G.; Chasseau, D.; Kahn, O. *J. Am. Chem. Soc.* **1997**, *119*, 10861.
(20) Kondo, A.; Kajiro, H.; Noguchi, H.; Carlucci, L.; Proserpio, D. M.; Ciani, G.; Kato, K.; Takata, M.; Seki, H.; Sakamoto, M.; Hattori, Y.; Okino, F.; Maeda, K.; Ohba, T.; Kaneko, K.; Kanoh, H. *J. Am. Chem. Soc.* **2011**, *133*, 10512.
(21) Zhang, J. P.; Lin, Y. Y.; Zhang, W. X.; Chen, X. M. *J. Am. Chem. Soc.* **2005**, *127*, 14162.
(22) Lin, J.-B.; Zhang, J.-P.; Chen, X.-M. *J. Am. Chem. Soc.* **2010**, *132*, 6654.
(23) Fu, A. Y.; Jiang, Y. L.; Wang, Y. Y.; Gao, X. N.; Yang, G. P.; Hou, L.; Shi, Q. Z. *Inorg. Chem.* **2010**, *49*, 5495.

(24) Lin, J.-B.; Zhang, J.-P.; Zhang, W.-X.; Xue, W.; Xue, D.-X.; Chen, X.-M. *Inorg. Chem.* **2009**, *48*, 6652.

(25) Bao, X.; Guo, P. H.; Liu, W.; Tucek, J.; Zhang, W. X.; Leng, J. D.; Chen, X. M.; Gural'skiy, I.; Salmon, L.; Bousseksou, A.; Tong, M. L. *Chem. Sci.* **2012**, *3*, 1629.

(26) Browne, E. J. *Aust. J. Chem.* **1975**, *28*, 2543.

(27) Sheldrick, G. M. *SADABS*; University Göttingen: Göttingen, Germany, 2002.

(28) Sheldrick, G. M. *SHELXTL*; Bruker Analytical Instrumentation: Madison, WI, 2000.

(29) Garcia, Y.; Kahn, O.; Rabardel, L.; Chansou, B.; Salmon, L.; Tuchagues, J. P. *Inorg. Chem.* **1999**, *38*, 4663.

(30) Grunert, C. M.; Schweifer, J.; Weinberger, P.; Linert, W.; Mereiter, K.; Hilscher, G.; Muller, M.; Wiesinger, G.; van Koningsbruggen, P. J. *Inorg. Chem.* **2004**, *43*, 155.

(31) Bonnet, S.; Siegler, M. A.; Costa, J. S.; Molnar, G.; Bousseksou, A.; Spek, A. L.; Gamez, P.; Reedijk, J. *Chem. Commun.* **2008**, 5619.

(32) Bonnet, S.; Molnar, G.; Costa, J. S.; Siegler, M. A.; Spek, A. L.; Bousseksou, A.; Fu, W. T.; Gamez, P.; Reedijk, J. *Chem. Mater.* **2009**, *21*, 1123.

(33) Martinez, V.; Gaspar, A. B.; Munoz, M. C.; Bukin, G. V.; Levchenko, G.; Real, J. A. *Chem.—Eur. J.* **2009**, *15*, 10960.

(34) Hayami, S.; Gu, Z. Z.; Yoshiki, H.; Fujishima, A.; Sato, O. *J. Am. Chem. Soc.* **2001**, *123*, 11644.

(35) Adams, C. J.; Muñoz, M. C.; Waddington, R. E.; Real, J. A. *Inorg. Chem.* **2011**, *50*, 10633.

(36) Koudriavtsev, A. B.; Stassen, A. F.; Haasnoot, J. G.; Grunert, M.; Weinberger, P.; Linert, W. *Phys. Chem. Chem. Phys.* **2003**, *5*, 3666.

(37) Koudriavtsev, A. B.; Stassen, A. F.; Haasnoot, J. G.; Grunert, M.; Weinberger, P.; Linert, W. *Phys. Chem. Chem. Phys.* **2003**, *5*, 3676.

(38) Rodriguez-Velamazan, J. A.; Carbonera, C.; Castro, M.; Palacios, E.; Kitazawa, T.; Letard, J. F.; Burriel, R. *Chem.—Eur. J.* **2010**, *16*, 8785.

(39) Brewer, C. T.; Brewer, G.; Butcher, R. J.; Carpenter, E. E.; Schmiedekamp, A. M.; Schmiedekamp, C.; Straka, A.; Viragh, C.; Yuzefpolskiy, Y.; Zavalij, P. *Dalton Trans.* **2011**, *40*, 181.

(40) Sugiyarto, K. H.; McHale, W. A.; Craig, D. C.; Rae, A. D.; Scudder, M. L.; Goodwin, H. A. *Dalton Trans.* **2003**, 2443.

(41) Kepenekian, M.; Le Guennic, B.; Robert, V. *Phys. Rev. B* **2009**, *79*, 094428.

(42) Guionneau, P.; Marchivie, M.; Bravic, G.; Letard, J.-F.; Chasseau, D. *Top. Curr. Chem.* **2004**, *234*, 97.

(43) Amoore, J. J. M.; Neville, S. M.; Moubaraki, B.; Iremonger, S. S.; Murray, K. S.; Letard, J. F.; Kepert, C. J. *Chem.—Eur. J.* **2010**, *16*, 1973.

(44) Martinez, V.; Gaspar, A. B.; Munoz, M. C.; Ballesteros, R.; Ortega-Villar, N.; Ugalde-Saldivar, V. M.; Moreno-Esparza, R.; Real, J. A. *Eur. J. Inorg. Chem.* **2009**, 303.

(45) Tang, J.; Sánchez Costa, J.; Smulders, S.; Molnár, G. b.; Bousseksou, A.; Teat, S. J.; Li, Y.; van Albada, G. A.; Gamez, P.; Reedijk, J. *Inorg. Chem.* **2009**, *48*, 2128.

(46) Gutlich, P.; Ksenofontov, V.; Gaspar, A. B. *Coord. Chem. Rev.* **2005**, *249*, 1811.

(47) Li, B.; Wei, R. J.; Tao, J.; Huang, R. B.; Zheng, L. S.; Zheng, Z. P. *J. Am. Chem. Soc.* **2010**, *132*, 1558.

(48) Ksenofontov, V.; Gaspar, A. B.; Gutlich, P. *Top. Curr. Chem.* **2004**, *235*, 23.

(49) Chernyshov, D.; Hostettler, M.; Tornroos, K. W.; Burgi, H. B. *Angew. Chem., Int. Ed.* **2003**, *42*, 3825.

(50) Griffin, M.; Shakespeare, S.; Shepherd, H. J.; Harding, C. J.; Letard, J. F.; Desplanches, C.; Goeta, A. E.; Howard, J. A. K.; Powell, A. K.; Mereacre, V.; Garcia, Y.; Naik, A. D.; Muller-Bunz, H.; Morgan, G. G. *Angew. Chem., Int. Ed.* **2011**, *50*, 896.

(51) Fletcher, A. J.; Thomas, K. M. *Langmuir* **2000**, *16*, 6253.

9430

dx.doi.org/10.1021/ic301237p | *Inorg. Chem.* 2012, 51, 9423–9430